Free-energy model for nanoparticle self-assembly by liquid crystal sorting

Noé Atzin,* Orlando Guzmán,† and Oscar Gutiérrez
Departamento de Física, Universidad Autónoma Metropolitana, Av. San Rafael Atlixco 186, Iztapalapa, Ciudad de México, 09340, México

Linda S. Hirst and Sayantani Ghosh
School of Natural Sciences, University of California, Merced, California 95343, USA

(Received 20 October 2017; revised manuscript received 16 May 2018; published 15 June 2018)

We modeled the experimentally observed self-assembly of nanoparticles (NPs) into shells with diameters up to 10 μm, via segregation from growing nematic domains. Using field-based Monte Carlo simulations, we found the equilibrium configurations of the system by minimizing a free-energy functional that includes effects of excluded-volume interactions among NPs, orientational elasticity, and the isotropic-nematic phase-transition energy. We developed a Gaussian-profile approximation for the liquid crystal (LC) order-parameter field that provides accurate analytical values for the free energy of LC droplets and the associated microshells. This analytical model reveals a first-order transition between equilibrium states with and without microshells, governed mainly by the competition of excluded-volume and phase-transition energies. By contrast, the LC elasticity effects are much smaller and mostly confined to setting the size of the activation barrier for the transition. In conclusion, field-based thermodynamic methods provide a theoretical framework for the self-assembly of NP shells in liquid crystal hosts and suggest that field-based kinetic methods could be useful to simulate and model the time evolution of NP self-assembly coupled to phase separation.

DOI: 10.1103/PhysRevE.97.062704

I. INTRODUCTION

Nanoparticles (NPs) exhibit unique electronic, magnetic, and optical properties arising from quantum confinement that (coupled with a large diversity in composition and morphology) find wide application in optoelectronics, biomedicine, food processing, and renewable energy [1–3].

A relatively new development is to use NPs as "building blocks" to assemble new structures with functionalities significantly modified from those of individual constituents [4]. The most common approaches include bottom-up assembly of NPs, which has successfully created two- and three-dimensional superlattices with up to three different types of particles and the synthesis of hybrid core-shell composite nanostructures [5–8]. An alternative route is to use soft materials (such as polymers, liquid crystals, or biomolecules) as templates for NP assembly [9–15]. A soft host can remove constraints in the way the individual components can be combined and make novel architectures possible, such as nonplanar structures. Additionally, it allows *in situ* modulation of the NP assembly via external controls (e.g., temperature, mechanical strain, and electromagnetic fields)[16–19].

Liquid crystals (LCs) are an ideal class of materials to serve as soft hosts for tunable assemblies, since their molecular structure can be modified by changing the temperature. Also, LCs can be manipulated to produce macroscopic domains with a defined optical axis, because their molecular orientation can be externally controlled by electric and magnetic fields and surface anchoring. This means that they can act as a switchable host for dynamic NP assembly and function. Our group has recently demonstrated examples of this ability by reorienting chains of quantum dots using a nematic host [20], modulating quantum-dot emission from a LC device [21–23], and using a liquid crystal host to reversibly modulate the emission intensity of quantum dot and magnetic NP clusters [13,24–26].

In this work we focus on a particular form of phase separation, previously reported by our group [27], that occurs when a homogeneous mixture of mesogen-functionalized NPs and 5CB molecules is cooled below the isotropic-nematic transition temperature: first [Fig. 1(a)], the NPs segregate into shrinking isotropic domains, where the particles remain uniformly distributed; in a second stage [Fig. 1(b)], these domains adopt a spherical shape. Finally [Fig. 1(c)], shells of closely packed NPs are formed when the interior of these spherical domains also becomes nematic (see electronic Supplemental Material for the article by Rodarte *et al.* [27]), pushing the particles to the droplet boundary. Careful observation of this interior domain formation indicate that the nematic phase nucleates and grows at a random point inside the isotropic domain away from the phase boundary. The shells vary in diameter from 200 nm up to $\sim$10 μm. Once formed, the shells can be extracted from the host LC phase and resuspended in an alternate organic solvent (for instance, toluene). This structural stability extends to high temperatures, but the shells break apart and NPs redisperse at temperatures between 115 °C and 125 °C [27].

Why do NP shells form at all, when there is a nematic liquid crystal at either side of the shell? In this work we provide a thermodynamic model with a first-order transition that accounts for the formation of these shells.

*noe.atzin@gmail.com
†ogl@xanum.uam.mx

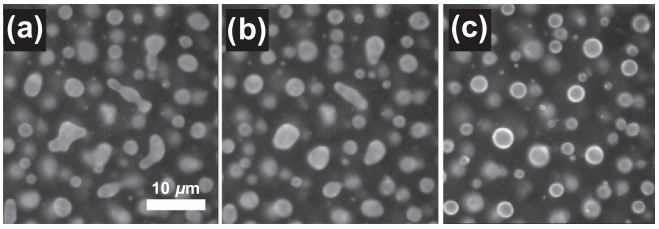

FIG. 1. The spatial organization of quantum-dot nanoparticles sorted by a liquid crystal is visualized using fluorescence microscopy. The images above were captured during the shell formation process. In the first stage (a), the NPs segregate into shrinking isotropic domains; at a later stage (b), these domains adopt a spherical shape; in the last stage (c), shells of NPs are formed when the interior of these spherical domains also becomes nematic.

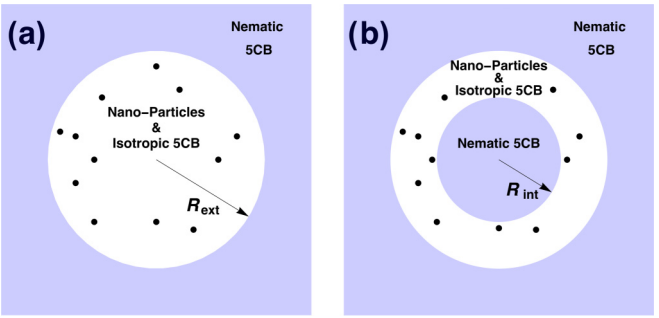

FIG. 2. We study a model where (a) nematic 5CB surrounds a sphere of isotropic 5CB with NPs suspended homogeneously inside it. The radius of that sphere $R_{\rm ext}$ is fixed. Then, (b) we analyze the free energy of the system when a droplet of nematic 5CB, with varying radius $R_{\rm int}$, confines the NPs to a shell of width $\Delta R = R_{\rm ext} - R_{\rm int}$.

When particles with a spherical geometry are introduced into a liquid crystal solvent, their ability to disperse depends on several factors: their size, the order parameter of the host phase, and the molecular anchoring conditions on the particle surface (for example, particle ligands and their orientation). A liquid crystal fluid can therefore be a good or bad solvent for spherical particles. In the case that the liquid crystal is a poor solvent, the particles tend to cluster and precipitate. In the limit of very small particles (∼1 nm or less), dispersal is favored in both the isotropic and nematic phases as these particles are too small to respond to the liquid crystal ordering. As size increases, however, particles tend to exhibit a reduced dispersibility in the nematic phase and will aggregate. This aggregation effect results from the Frank elastic energy cost per particle to place a particle with spherical geometry in a nematic environment, thereby distorting the equilibrium director field.

NPs larger than a few nanometers coated with nonmesogenic ligands have been shown experimentally to aggregate in the nematic phase [28–30]. The specific nanoparticles (6-nm quantum dots) used in the experiments of Rodarte *et al.* include mesogenic ligands attached to the particle surface via a flexible arm. While these mesogenic particles do not disperse in the nematic phase (possibly due to elastic-energy costs [31,32] or electrostatic effects [33]), they do disperse homogenoeously in the isotropic phase of 5CB [27]. Hence, in our model, we assume that the NPs have great affinity for the isotropic phase [7,28,34–36] (see Fig. 2). Transport of particles and clusters by isotropic-nematic domain walls has been reported previously [37,38], but since we are considering only the thermodynamics we do not model such transport explicitly.

When the system initially phase separates into NP-rich isotropic domains and NP-poor nematic domains, we observe a time-dependent length scale associated with the cooling rate, and that faster cooling rates lead to smaller shells. Such behavior noted previously by Rodarte *et al* . [27] has also been observed computationally for the isotropic-nematic transition without nanoparticles [39] and attributed to the interplay between symmetry breaking and causality described by the Kibble-Zurek mechanism [40,41]. The relationship between cooling rate and final shell size will be discussed in detail in a separate publication [42]. High speed movies of shell formation (available as Supplemental Material for [27]) show that shrinking isotropic droplets reach a final outer radius $R_{\rm ext}$ before nucleation of the inner nematic domain, during which time $R_{\rm ext}$ does not appear to change. Hence, in this work we analyze the system starting from the second stage [Fig. 1(b)], considering a spherical domain of given radius $R_{\rm ext}$. This sphere contains, initially, NPs distributed homogeneously at a volume fraction η_0. We then consider the free energy of the system when a nematic droplet of radius $R_{\rm int}$ is located at the center of the spherical domain. We assume that the nematic phases inside and outside the original spherical domain confine the NPs to the region between them, and develop a mean-field theory model for the free energy of the shell and the nematic droplet.

In the model, we include the elastic and Landau-de Gennes free energies for the nematic droplet and the excluded-volume free energy of NPs considered as hard spheres. The excluded-volume term favors small values of $R_{\rm int}$, while the other two terms favor larger ones. An equilibrium droplet radius $R_{\rm int} > 0$ is found for sufficiently low temperature quenches, $\Delta T = T - T_c$, where $T_c = 308$ K is the isotropic-nematic transition temperature for 5CB [43].

In the next sections, we describe in detail our free-energy model for the formation of NP shells in a nematic host and use Monte Carlo simulation to find accurate expressions for each of the free-energy contributions mentioned above. Then we use those expressions to calculate the equilibrium droplet radius $R_{\rm int}$ as a function of the temperature quench ΔT and the initial NP volume fraction η_0. We discuss the presence of a first-order transition that leads to formation of shells and identify the role of the excluded-volume and phase-transition free energies in setting the shell thickness $\Delta R = R_{\rm ext} - R_{\rm int}$. We also discuss the role that the elastic energy has in setting the activation energy that must be overcome in order to nucleate the inner droplet and associated shell. In the conclusions we consider other systems where similar competition between excluded-volume interactions and phase-transition heat could lead to formation of self-assembled structures.

II. METHODS

A. Model for the microshell and nematic droplet

We assume that the system contains an inner nematic droplet with radius $R_{\rm int}$ and that the NPs are confined to an external

shell where 5CB remains isotropic [see Fig. 2(b)]. The outer size of the spherical domain is known experimentally to be set by the cooling rate of the system, and is related to the process of growth and coarsening of the nematic phase network around the shrinking isotropic domains containing NPs [42]. We also assume infinitely strong anchoring at the shell boundary and model the excess free energy of the system $\mathcal{F}$ with respect to the situation where $R_{\rm int} = 0$. Then, $\mathcal{F}$ is the sum of three volumetric terms:

$$\mathcal{F} = \int_{\rm shell} f_{\rm NP} d\mathbf{X} + \int_{\rm droplet} (f_{\rm E} + f_{\rm I\text{-}N}) d\mathbf{X}. \quad (1)$$

Here, $f_{\rm NP}$ is the free-energy density due to excluded volume of the NPs dispersed in the shell and $\mathbf{X}$ is a point of the domain. For the liquid crystal in the inner droplet, $f_{\rm E}$ is the elastic free-energy density and $f_{\rm I\text{-}N}$ is a Landau-de Gennes free-energy density accounting for the isotropic-nematic transition.

We model the NP free-energy density with the Carnahan-Starling expression for hard spheres [44]. The NP volume fraction is assumed to be constant over the whole shell; it is an increasing function of the inner droplet radius,

$$\eta(R_{\rm int}) = \frac{\eta_0}{1 - (R_{\rm int}/R_{\rm ext})^3}. \quad (2)$$

The state of the liquid crystal in the nematic droplet is described by the alignment tensor field $\mathbf{Q}(\mathbf{X})$: At each point $\mathbf{X}$, it corresponds to the local average $\mathbf{Q} = \langle \hat{\mathbf{u}}\hat{\mathbf{u}} - \mathbf{I}/3 \rangle$, where $\hat{\mathbf{u}}$ represents the molecular orientation and $\mathbf{I}$ is the identity matrix. The scalar order parameter is given by $S = 3\lambda_1/2$, with λ_1 the largest eigenvalue of $\mathbf{Q}$, and the director $\hat{\mathbf{n}}$ is the unit eigenvector associated with λ_1. One advantage of using the alignment tensor as the order parameter is that the elastic free energy does not diverge at topological defects, because the derivatives of $\mathbf{Q}$ are continuous [45,46].

We defined nondimensional quantities using, as the unit of length, the external radius $R_{\rm ext}$ and, as the unit of energy, the latent heat ϵ required to bring a sphere of radius $R_{\rm ext}$ from the nematic to the isotropic phase, at 1 K below the clearing point:

$$\epsilon = -\frac{4\pi R_{\rm ext}^3}{3} f_{\rm I\text{-}N}(\Delta T = -1\ {\rm K}). \quad (3)$$

Hence, we use the following reduced quantities: coordinates $\mathbf{x} = \mathbf{X}/R_{\rm ext}$, internal-droplet radius $r = R_{\rm int}/R_{\rm ext}$, free-energy $F = \mathcal{F}/\epsilon$, and free-energy densities,

$$f_{\rm NP}^* = \frac{6k_B T}{\pi\epsilon}\left(\frac{R_{\rm ext}}{\sigma}\right)^3 \left[\frac{\eta^2(4-3\eta)}{(1-\eta)^2}\right], \quad (4)$$

$$f_{\rm E}^* = \frac{L_1 R_{\rm ext}}{\epsilon}\left[\frac{1}{2}\frac{\partial Q_{jk}}{\partial x_l}\frac{\partial Q_{jk}}{\partial x_l}\right], \quad (5)$$

$$f_{\rm I\text{-}N}^* = \frac{L_1 R_{\rm ext}}{\epsilon}\left(\frac{R_{\rm ext}^2}{\xi^2}U\right)\left[\left(\frac{1}{U} - \frac{1}{3}\right)\frac{{\rm Tr}\mathbf{Q}^2}{2} - \frac{{\rm Tr}\mathbf{Q}^3}{3} + \frac{({\rm Tr}\mathbf{Q}^2)^2}{4}\right]. \quad (6)$$

In these equations, $k_{\rm B}$ is Boltzmann constant, T temperature, σ the NP diameter, L_1 an elastic modulus related to the Frank elastic constant K_{11} by $L_1 = 2K_{11}/S^2$ in the one-constant approximation, ξ is the bare coherence length of the nematic, and U is a parameter related to the bulk order parameter by $U = 3/(1 + S_b - S_b^2)$. In turn, the bulk order parameter was related to the temperature quench ΔT by fitting experimental data for 5CB [43],

$$S_{\rm b} = 0.352 - 10.417\,\frac{\Delta T}{T_c} - 112.213\left(\frac{\Delta T}{T_c}\right)^2. \quad (7)$$

From the experiments by Rodarte *et al.* [27], we set $R_{\rm ext} = 1\ \mu$m and $\sigma = 5$ nm as typical values, along with $\xi = 10$ nm and $L_1 = 10^{-11}$ N which are typical for nematics [47].

B. Monte Carlo simulation of the droplet

The integration of the NP free-energy density can be performed analytically by assuming that the NP volume fraction is uniform over the shell region, but calculation of the LC terms over the nematic droplet requires the field $\mathbf{Q}(\mathbf{x})$. We used a simulated-annealing Monte Carlo methodology to obtain it, where the variables subject to random variation are the five independent components of the alignment tensor [48,49]. By using these degrees of freedom, we were able to sample configurations where the order parameters S and B, as well as the director $\hat{\mathbf{n}}$ and second optical axis $\hat{\mathbf{m}}$, may vary simultaneously in space.

Further details about the simulations are given as Supplemental Material [50], but we mention here that we carried out them by taking advantage of the cylindrical symmetry of the expected equilibrium configurations for homeotropic anchoring (uniform, axial, and radial [51,52]). We represented the state of the whole droplet using just a slice of the $\mathbf{Q}$ field in the xz plane containing the axis of symmetry. While this slice is two-dimensional, our calculations still evaluated integrations over the entire three-dimensional domain and, since $\mathbf{Q}$ still had five degrees of freedom, the director associated with it was not restricted to lie on the xz slice. We validated this method by performing fully three-dimensional simulations: As described in the Supplemental Material, we found that they agree within 2%, 1%, and 0.1% for droplets with $R_{\rm ext} = 200$, 300, and 400 nm, respectively.

Figure 3 illustrates the annealing protocol (for a droplet with $r = 0.2$, $S_{\rm b} = 0.5$, and strong radial anchoring), showing initial, intermediate, and final configurations. We checked that the final free energy after three annealing steps was insensitive to the initial configuration being random, uniform with $S(\mathbf{x}) = 0$ or uniform with $S(\mathbf{x}) = S_{\rm b}$, and constant director.

III. RESULTS

A. A Gaussian-profile model for the order-parameter field accounts for the topological defect in the nematic droplet

For strong homeotropic anchoring at the edge of the nematic droplet, the equilibrium configurations obtained in our simulations correspond to uniaxial hedgehog defects [51,52], as shown in Fig. 3. The biaxiality parameter in these configurations is very small; its r.m.s. value is lower than 0.001. This allows one to represent the final, equilibrium configurations with a radial director configuration $\hat{\mathbf{n}}(\mathbf{x}) = \hat{\mathbf{x}}$ and a radial profile of the scalar order parameter $S(x)$ as shown in Fig. 4.

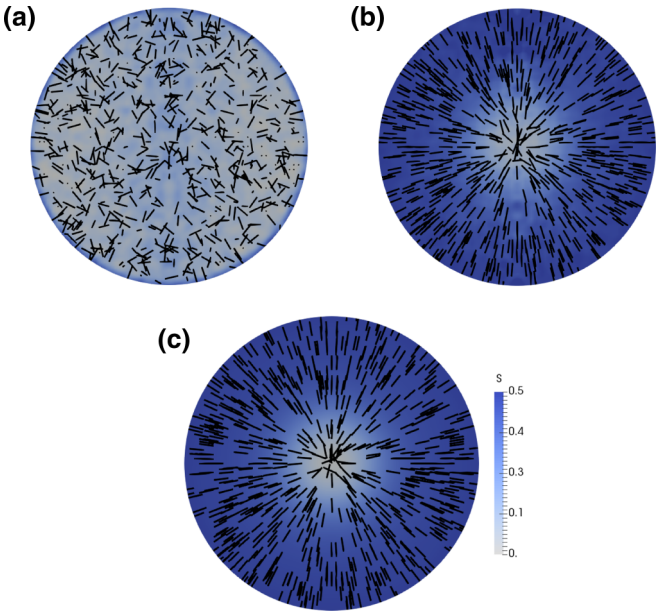

FIG. 3. We performed simulated annealing to find the inner-nematic droplet configuration that minimizes its free energy. For the case with reduced inner radius $r = 0.2$, $S_b = 0.5$, and strong radial anchoring, we show (a) the initial random configuration, (b) the equilibrated configuration after the first annealing run, and (c) the final equilibrated configuration after the second (and last) annealing run. The simulation shows that the order-parameter field $S(\mathbf{x})$ is inhomogeneous due to the presence of a central hedgehog defect.

Figure 4 also shows that $S(x)$ for the different radii can be approximated well by a single Gaussian profile:

$$S(x) = S_{\text{bulk}}(1 - e^{-x^2/d^2}), \tag{8}$$

where d represents the width of the defect-core region. A fit to a subset of our simulation data (for $r = 0.2, 0.3$, and 0.4, and $S_b = 0.39$ and 0.60), results in the following parametrization:

$$d(S_b) = 0.267 - 0.367 S_b. \tag{9}$$

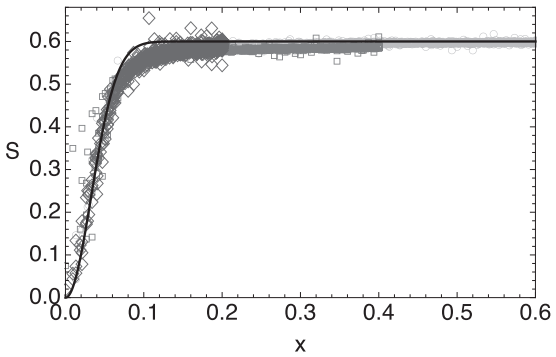

FIG. 4. The order-parameter profile $S(x)$ as a function of the radial coordinate x is shown for nematic droplets with varying radius $r = 0.2$ (dark gray diamonds), 0.4 (gray squares), and 0.6 (light gray circles), at $T = 294$ K with bulk order parameter $S_b = 0.6$. The solid line corresponds to the analytical model of $S(x)$ given in Eq. (8), which is independent of the droplet size.

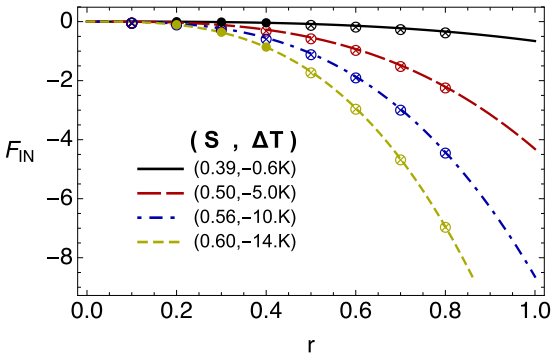

FIG. 5. The phase-transition free energy F_{IN} is a decreasing function of droplet radius r: Simulation results are shown as circles, with solid ones indicating those used to fit Eq. (9). The analytical free energy from Eq. (11), shown with lines, remains accurate even when extrapolated to the largest simulated droplets. The range of S_b and ΔT cover the experimental range between crystallization and isotropic-nematic transition.

Combining Eqs. (8) and (9) with a radial director field, we obtain an analytical model for the equilibrium $\mathbf{Q}$ tensor field:

$$\mathbf{Q} = S(x)(\hat{\mathbf{x}}\hat{\mathbf{x}} - \mathbf{I}/3). \tag{10}$$

B. Analytical expressions of the free-energy terms reproduce accurately the simulation results

We calculated analytically the total phase-transition and elastic free energies by integration of the corresponding densities, using the $\mathbf{Q}$ field given by Eq. (10) and computer-algebra software [53]. The general results are given in the Supplemental Material [50], but for droplets much larger than the defect core, $r \gg d$, they simplify to

$$F_{\text{IN}} = \left(\frac{L_1 R_{\text{ext}}^3}{\epsilon \xi^2}\right)\frac{4\pi r^3 S_b^3}{3}\left[\frac{1 - 3S_b}{27}\right] \tag{11}$$

$$F_{\text{E}} = \left(\frac{L_1 R_{\text{ext}}}{\epsilon}\right)8\pi r S_b^2\left[1 - \sqrt{\pi}\left(1 - \frac{11\sqrt{2}}{32}\right)\frac{d}{r}\right]. \tag{12}$$

These closed expressions for the free energies can be evaluated for the entire range of interest of radius r and temperature quench ΔT (and corresponding S_b). To cover the experimentally accessible temperature range (between the clearing point and the crystallization temperature of 5CB), we need to consider values of ΔT as low as -13.6 ± 0.5 K [43,54,55] and, correspondingly, values of S_b up to 0.60.

Figures 5 and 6 compare the closed expressions and simulated values for the phase- transition and elastic free energies. They agree very well over the entire size and temperature ranges: The total free energy of the nematic droplet calculated analytically has a r.m.s. difference of 5% with respect to the simulation data. Given this level of agreement, in the next sections we will mainly discuss the formation of NP microshells using the analytical free-energy expressions of Eqs. (11) and (12), but will be able to make comparisons with simulation results.

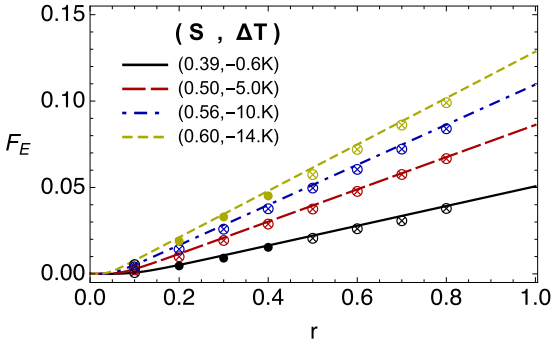

FIG. 6. The elastic free energy F_{E} is an increasing function of droplet size r. As in Fig. 5, the analytical free energy from Eq. (12), shown with lines, is in good agreement with simulation results (circles). Again, solid circles indicate simulations used to fit Eq. (9).

C. A first-order transition leads to shell formation

To obtain the total free energy of the system, we added the analytical free energies for the nematic droplet and the Carnahan-Starling contribution from the shell. Figure 7 illustrates the scale for each contribution: The positive NP contribution is the larger one, growing steeply with the radius r. The phase-transition contribution is the second largest in magnitude and of the opposite sign, while the elastic one is the smallest. From this, we see that the free-energy minima will be set mainly from a competition between the LC phase-transition energy and the NP excluded-volume free-energy terms. The LC elasticity contribution will be of secondary importance for the mechanism leading to the NP shells and, therefore, details about the anchoring type and strength (as well as the detailed director configuration inside the LC droplet) become less pressing for determining the mechanism behind the formation of the NP shells.

Figure 8 shows the total free energy of the system $F(r)$ as a function of the LC droplet radius, for three different

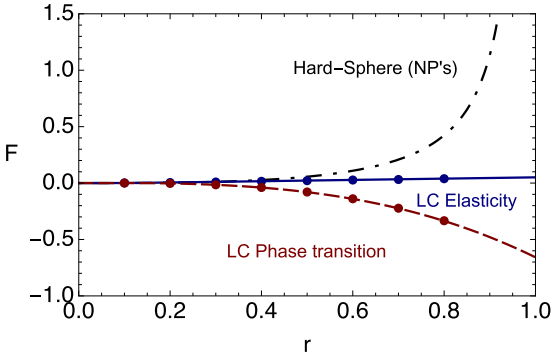

FIG. 7. The excluded-volume (black dot-dashed line), elastic (blue solid line), and phase-transition (dashed line) contributions to the total free energy of the system scale very differently with inner droplet radius r: While the elastic contribution grows slowly with increasing r, the hard-sphere and phase-transition terms grow quickly and have opposite signs. The lines correspond to analytical expressions for the free energies, while Monte Carlo simulation data are shown as points, for the case with $\Delta T = -0.6$ K and initial NP volume fraction $\eta_0 = 0.02$.

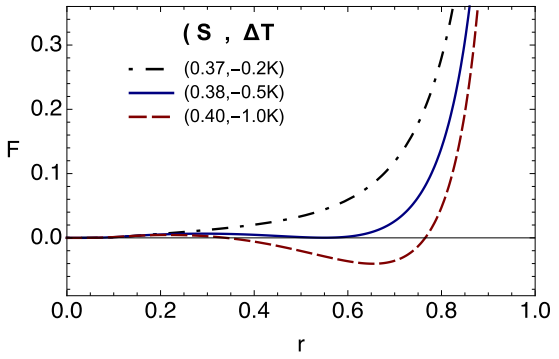

FIG. 8. A first-order structural transition is found for temperatures sufficiently below the clearing point T_c: At $\Delta T = (T - T_c) = -0.5$ (blue solid line) the free energy for the minimum with $r > 0$ is the same as that with the system with no shell formed ($r = 0$). At lower temperatures, e.g., $\Delta T = -1.0$ (red dashed line) the global minimum is the state $r > 0$, that is, the state with a shell is favored thermodynamically. For sufficiently high temperatures, such as $\Delta T = -0.5$ (black dot-dashed line) the only minimum is at $r = 0$ and no shell would be formed.

temperatures at initial NP volume fraction $\eta_0 = 0.02$. We observe that there is a first-order transition at $\Delta T_{\mathrm{shell}} = -0.5$ K, when the free energy at a minimum with $r > 0$ becomes equal to zero. For higher temperatures, the thermodynamically stable state is the one with $r = 0$ (no nematic droplet and hence no shell). As ΔT is lowered below -0.5 K, the stable state corresponds to larger-radius droplets and thinner shells.

Figure 9 displays this first-order transition by plotting the equilibrium radius $r_{\mathrm{eq}}(\Delta T)$ as a function of the quench ΔT for the constant NP fraction η_0: Just below the clearing point, the stable state is an isotropic drop. When the temperature quench decreases below $\Delta T_{\mathrm{shell}}$ there is a discontinuity in the equilibrium radius and suddenly a nematic droplet and the NP shells are formed. The equilibrium radii in Fig. 9 were obtained from analytical expressions in Eqs. (11) and (12), but we also calculated them by interpolation of the free energies

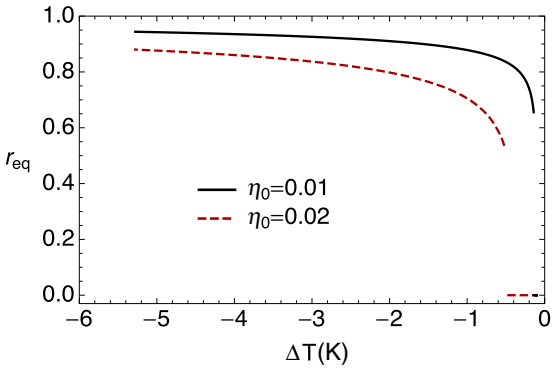

FIG. 9. The equilibrium radius as a function of the temperature difference $\Delta T = (T - T_c)$ decreases as the initial NP volume fraction increases (that is, the shells thicken as η_0 grows). The first-order transition point $\Delta T_{\mathrm{shell}}$ also decreases with increasing η_0: Lower temperatures are needed in order to form a stable shell as one increases the initial volume fraction of NPs (lower and higher volume fraction curves indicated by black solid and red dashed lines, respectively).

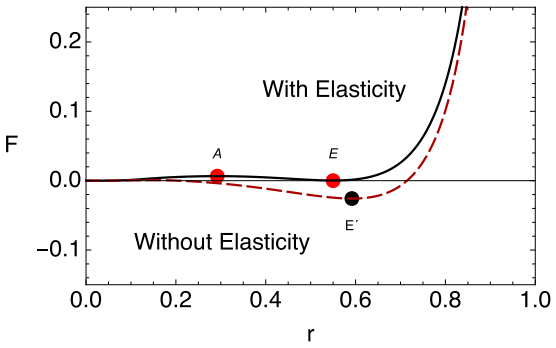

FIG. 10. The equilibrium radius is set mainly by competition between the NP excluded-volume and LC phase-transition free energies. The total free energy (black solid line) displays an equilibrium point E and an activated state A. If one neglects the LC elasticity term (red dashed line), the new equilibrium point E′ is shifted by 8% to the right of E and the barrier to formation of shells is lowered.

at those temperatures at which we performed simulations. The difference between r_{eq} obtained from simulation and from the analytical model was found to be quite small (less than 0.04% for $\Delta T < -5.0$ K, and less than 3% at $\Delta T = -0.6$ K, the temperature of our simulations closest to the transition point.)

The range of equilibrium shell thickness displayed in Fig. 9 corresponds to the experimental thickness observed by Rodarte *et al.* [27]. In the same figure, we see that the effect of increasing the initial NP volume fraction is to lower the transition point ΔT_{shell}, as well as to enlarge the shell thickness. We have thus identified two experimental variables that control the formation and thickness of the NP shells: the quench temperature and the initial NP concentration. Analyzing the function $r_{eq}(\Delta T, \eta_0)$ at constant ΔT, one finds that the thickness of the shell increases with η_0 (as one would expect). The transition manifests then as a threshold value $\eta_{0,max}$ above which no shells can be formed, as the equilibrium radius jumps discontinuously to zero (this behavior is illustrated in the Supplemental Material [50]).

D. The activation barrier is set by LC elasticity

Since shell formation corresponds to a first-order transition, we can expect hysteresis associated with the crossing of an activation barrier. This barrier is illustrated in Fig. 10, with the activated and equilibrium states labeled as A and E, respectively. The same figure shows that most of the barrier is contributed by the elastic energy, by showing the effect of neglecting the latter quantity that scales linearly with r. (This would be the case also for other director configurations, such as the bipolar texture associated with planar anchoring conditions.) Hence, the barrier-crossing kinetics will be affected sensitively by the LC elasticity and one may control the formation rate of the shells through the elastic constants and surface anchoring coefficient of the liquid crystal. Also of notice is that the nematic-droplet radius corresponding to the activated state is about 300 nm. This is much larger than the estimated size (of a few nanometers) of critical nuclei for homogeneous nucleation of liquid water from its vapor [56]. Such relatively large size may allow measurements of nucleation kinetics as a function of the barrier height using light scattering techniques or by high speed fluorescence imaging.

IV. CONCLUSION

We have provided a first-order structural-transition framework to study the assembly of nanoparticle shells by liquid crystal sorting. The free energy from excluded-volume interactions between the NPs competes with the change in free energy due to the isotropic-nematic phase transition: The former drives a thicker NP shell while the latter favors a thinner one, so that an equilibrium thickness is eventually achieved. The effects of LC elasticity are much smaller and manifest chiefly in controlling the height of the activation barrier between the states with and without shells.

We obtained closed expressions for the Landau-de Gennes and elastic free energies by parametrizing the order-parameter field of the inner nematic droplet with a radial director and Gaussian profile for the nematic order parameter. These closed expressions account successfully for the results of our field-based Monte Carlo simulations and the experimentally observed behavior of formation of shells at temperatures below the isotropic-nematic transition of 5CB.

We expect that a field-based simulation could be useful in describing the initial phase-separation sorting process, where pure-nematic domains grow inside the isotropic mixture if NPs and 5CB. We are currently modeling such a kinetic separation process [42], involving fields with and without conservations laws, as in model C of the classification of Hohenberg and Halperin of dynamic critical phenomena [57].

We also expect that field-based models of self-assembly driven by phase or structural transitions would be useful to search for other morphologies of aggregation besides the spherical one. Cylinders and lamellae could also be attainable by tuning the interactions among NPs and different soft-matter hosts. As possibilities for such cooperative self-assembly hosts, we can mention smectic [58] and cholesteric liquid crystals [48], as well as polymers and ionic liquids [16].

ACKNOWLEDGMENTS

N.A. acknowledges support from Universidad Autónoma Metropolitana for a Ph.D. scholarship. This project was funded by UC-MEXUS/Conacyt through the project "3D assembly of nanoparticles via liquid crystalline (LC) templates for the design and synthesis of responsive ("smart") multifunctional materials." This work was partly supported by National Science Foundation Grants No. PHY-1066293 and No. DMR-CBET-150755, the NSF-CREST, Center for Cellular and Biomolecular Machines (CCBM) at UC Merced (HRD-1547848), and Consejo Nacional de Ciencia y Tecnología (Mexico) Project "Fronteras de la Ciencia" 2015-02-1450.

[1] N.-M. Park, T.-S. Kim, and S.-J. Park, Appl. Phys. Lett. **78**, 2575 (2001).

[2] L. Zhuang, L. Guo, and S. Y. Chou, Appl. Phys. Lett. **72**, 1205 (1998).

[3] J. K. Jaiswal, H. Mattoussi, J. M. Mauro, and S. M. Simon, Nat. Biotechnol. **21**, 47 (2003).

[4] J. M. Costa-Fernández, R. Pereiro, and A. Sanz-Medel, Trends Anal. Chem. **25**, 207 (2006).

[5] A. J. Nozik, Physica E **14**, 115 (2002).

[6] E. V. Shevchenko, D. V. Talapin, N. A. Kotov, S. O'Brien, and C. B. Murray, Nature (London) **439**, 55 (2006).

[7] M. F. Prodanov, N. V. Pogorelova, A. P. Kryshtal, A. S. Klymchenko, Y. Mely, V. P. Semynozhenko, A. I. Krivoshey, Y. A. Reznikov, S. N. Yarmolenko, J. W. Goodby, and V. V. Vashchenko, Langmuir **29**, 9301 (2013).

[8] F. X. Redl, K.-S. Cho, C. B. Murray, and S. O'Brien, Nature (London) **423**, 968 (2003).

[9] S. Sun, C. B. Murray, D. Weller, L. Folks, and A. Moser, Science **287**, 1989 (2000).

[10] A. Dong, J. Chen, P. M. Vora, J. M. Kikkawa, and C. B. Murray, Nature (London) **466**, 474 (2010).

[11] R. Bitar, G. Agez, and M. Mitov, Soft Matter **7**, 8198 (2011).

[12] D. Coursault, J. F. Blach, J. Grand, A. Coati, A. Vlad, B. Zappone, D. Babonneau, G. Lévi, N. Félidj, B. Donnio, J. L. Gallani, M. Alba, Y. Garreau, Y. Borensztein, M. Goldmann, and E. Lacaze, ACS Nano **9**, 11678 (2015).

[13] M. A. Gharbi, S. Manet, J. Lhermitte, S. Brown, J. Milette, V. Toader, M. Sutton, and L. Reven, ACS Nano **10**, 3410 (2016).

[14] A. Tao, P. Sinsermsuksakul, and P. Yang, Nat. Nanotechnol. **2**, 435 (2007).

[15] S. A. Claridge, A. W. Castleman Jr., S. N. Khanna, C. B. Murray, A. Sen, and P. S. Weiss, ACS Nano **3**, 244 (2009).

[16] A. Hussain, A. T. S. Semeano, S. I. C. J. Palma, A. S. Pina, J. Almeida, B. F. Medrado, A. C. C. S. Pádua, A. L. Carvalho, M. Dionísio, R. W. C. Li, H. Gamboa, R. V. Ulijn, J. Gruber, and A. C. A. Roque, Adv. Funct. Mater. **27**, 1700803 (2017).

[17] T. Hegmann, H. Qi, and V. M. Marx, J. Inorg. Organomet. Polym. Mater. **17**, 483 (2007).

[18] M. Chambers, H. Finkelmann, M. Remskar, A. Sanchez-Ferrer, B. Zalar, and S. Zumer, J. Mater. Chem. **19**, 1524 (2009).

[19] Y. Lin, A. Daoudi, A. Segovia-Mera, F. Dubois, C. Legrand, and R. Douali, Phys. Rev. E **93**, 062702 (2016).

[20] Y. K. Verma, R. H. Inman, C. G. L. Ferri, H. Mirafzal, S. N. Ghosh, D. F. Kelley, L. S. Hirst, S. Ghosh, and W. C. Chin, Phys. Rev. B **82**, 165428 (2010).

[21] A. L. Rodarte, C. Gray, L. S. Hirst, and S. Ghosh, Phys. Rev. B **85**, 035430 (2012).

[22] A. L. Rodarte, G. V. Shcherbatyuk, L. Scherbatyuk, L. S. Hirst, and S. Ghosh, RSC Adv. **2**, 12759 (2012).

[23] A. L. Rodarte, R. J. Pandolfi, S. Ghosh, and L. S. Hirst, J. Mater. Chem. C **1**, 5527 (2013).

[24] J. J. Amaral, J. Wan, A. L. Rodarte, C. Ferri, M. T. Quint, R. J. Pandolfi, M. Scheibner, L. S. Hirst, and S. Ghosh, Soft Matter **11**, 255 (2015).

[25] R. K. Shukla, J. Mirzaei, A. Sharma, D. Hofmann, T. Hegmann, and W. Haase, RSC Adv. **5**, 34491 (2015).

[26] D. Kasyanyuk, P. Pagliusi, A. Mazzulla, V. Reshetnyak, Y. Reznikov, C. Provenzano, M. Giocondo, M. Vasnetsov, O. Yaroshchuk, and G. Cipparrone, Sci. Rep. **6**, 20742 (2016).

[27] A. L. Rodarte, B. H. Cao, H. Panesar, R. J. Pandolfi, M. Quint, L. Edwards, S. Ghosh, J. E. Hein, and L. S. Hirst, Soft Matter **11**, 1701 (2015).

[28] A. L. Rodarte, Z. S. Nuno, B. H. Cao, R. J. Pandolfi, M. T. Quint, S. Ghosh, J. E. Hein, and L. S. Hirst, Chem. Phys. Chem. **15**, 1413 (2014).

[29] P. G. Petrov and E. M. Terentjev, Langmuir **17**, 2942 (2001).

[30] D. Andrienko, M. Tasinkevych, P. Patrício, and M. M. Telo da Gama, Phys. Rev. E **69**, 021706 (2004).

[31] A. V. Ryzhkova and I. Muševič, Phys. Rev. E **87**, 032501 (2013).

[32] Y. Wang, P. Zhang, and J. Z. Y. Chen, Phys. Rev. E **96**, 042702 (2017).

[33] A. V. Ryzhkova, M. Škarabot, and I. Muševič, Phys. Rev. E **91**, 042505 (2015).

[34] G. L. Nealon, R. Greget, C. Dominguez, Z. T. Nagy, D. Guillon, J. L. Gallani, and B. Donnio, Beilstein J. Org. Chem. **8**, 349 (2012).

[35] J. Milette, V. Toader, E. R. Soulé, R. B. Lennox, A. D. Rey, and L. Reven, Langmuir **29**, 1258 (2013).

[36] M. Roohnikan, V. Toader, A. Rey, and L. Reven, Langmuir **32**, 8442 (2016).

[37] J. L. West, A. Glushchenko, G. Liao, Y. Reznikov, D. Andrienko, and M. P. Allen, Phys. Rev. E **66**, 012702 (2002).

[38] J. Cleaver and W. C. K. Poon, J. Phys.: Condens. Matter **16**, S1901 (2004).

[39] Z. Bradac, S. Kralj, and S. Zumer, J. Chem. Phys. **135**, 024506 (2011).

[40] T. W. B. Kibble, J. Phys. A.: Math. Gen. **9**, 1387 (1976).

[41] W. H. Zurek, Nature (London) **317**, 505 (1985).

[42] S. T. Riahinasab, A. Keshavarz, C. N. Melton, A. Elbaradei, G. I. Warren, R. L. Selinger, B. J. Stokes, and L. S. Hirst (unpublished).

[43] R. G. Horn, J. Phys. **39**, 105 (1978).

[44] N. F. Carnahan and K. E. Starling, J. Chem. Phys. **51**, 635 (1969).

[45] N. Schopohl and T. J. Sluckin, Phys. Rev. Lett. **59**, 2582 (1987).

[46] C. Chiccoli, P. Pasini, A. Sarlah, C. Zannoni, and S. Zumer, Phys. Rev. E **67**, 050703 (2003).

[47] S. Mkaddem and E. C. Gartland Jr., Phys. Rev. E **62**, 6694 (2000).

[48] J. C. Armas-Pérez, A. Londono-Hurtado, O. Guzmán, J. P. Hernández-Ortiz, and J. J. de Pablo, J. Chem. Phys. **143**, 044107 (2015).

[49] N. Atzin, Master's thesis, Universidad Autónoma Metropolitana-Iztapalapa, 2014.

[50] See Supplemental Material at http://link.aps.org/supplemental/10.1103/PhysRevE.97.062704 for details about the model, simulation methodology, and closed expressions for the elastic and phase-transition free energies.

[51] S. Kralj, S. Zumer, and D. W. Allender, Phys. Rev. A **43**, 2943 (1991).

[52] S. Kralj and E. G. Virga, J. Phys. A.: Math. Gen. **34**, 829 (2001).

[53] Wolfram Research Inc., *Computer code MATHEMATICA, Version 11.1* (Wolfram Research, Champaign, 2017).

[54] P. T. Mather, D. S. Pearson, and R. G. Larson, Liq. Cryst. **20**, 527 (1996).

[55] G. P. Sinha and F. M. Aliev, Phys. Rev. E **58**, 2001 (1998).

[56] J. R. Espinosa, C. Vega, C. Valeriani, and E. Sanz, J. Chem. Phys. **144**, 034501 (2016).

[57] P. C. Hohenberg and B. I. Halperin, Rev. Mod. Phys. **49**, 435 (1977).

[58] R. Pérez-Ortiz, O. Guzmán, and J. A. Reyes, Phys. Rev. E **84**, 011701 (2011).